Inverse Spin Hall Effect in Nonequilibrium Dirac Systems Induced by Anomalous Flow Imbalance

Hung-Hsuan Teh¹,* Tokiro Numasawa¹, Shun Okumura^{1,2}, and Takashi Oka^{1†}

¹The Institute of Solid State Physics, The University of Tokyo, Kashiwa, Chiba 277-8581, Japan

²Deperment of Applied Physics, The University of Tokyo, Hongo, Tokyo, 113-8656, Japan

(Dated: October 10, 2024)

We study Dirac fermions in the presence of a space-dependent chiral gauge field and thermodynamic gradients, establishing a connection to the inverse spin Hall effect. The chiral gauge field induces a chiral magnetic field, resulting in a surface Fermi arc state and a chiral Landau level state which, although is delocalized in the bulk, we show to be more robust against impurities. By applying chemical potential and temperature gradients, we achieve nonzero charge currents, with each gradient leading to distinct Fermi level dependencies, both of which have been observed in a recent experiment. Unlike the conventional mixed axial-gravitational anomaly, our currents require a noncollinear chiral magnetic field and thermodynamic gradient. We further derive low-energy transport formulas and demonstrate the importance of carefully treating the ultraviolet cutoff for understanding our lattice calculations.

Introduction — Quantum materials respond to external forces, exhibiting currents that are governed by symmetry properties and conservation laws. The presence of multiple symmetries can lead to intriguing cross-correlations among these currents. This has profound implications in the realm of spintronics where the interconnection between charge and spin currents has attracted attention, particularly in materials where electron spin orientation exhibits weak conservation. A prime illustration of this is the spin Hall effect, where an applied electric field induces not only a direct charge current but also a transverse spin current, showing a fundamental spin-charge interplay [1–5].

Conversely, the *inverse* spin Hall effect (ISHE) represents a less explored frontier, initially observed at the interface between a ferromagnetic electrode and platinum [6]. At the interface, a spin current injected into platinum results in a transverse charge current, underscoring the reciprocal nature of spin-charge conversion. Recently, a helicity-dependent transverse photo-excited current in bismuth based Dirac semimetals was measured [7]. This current distinguishes itself from conventional photocurrents, which typically flow parallel to the plane of incidence. Although there is no ferromagnetic electrode in the system, its origin is speculated to be the inverse spin Hall effect. In this scenario, circularly polarized light induces spin accumulation at the irradiated surface. This mirrors the magnetic proximity effect originally achieved with the ferromagnet. The sign and size of the photo-excited current depend sensitively on the electron density and its microscopic understanding is still an open issue.

From ISHE to Dirac Systems — In this paper we study a simplified model of current generation inspired by the ISHE scenario described in Ref. [7]. Concepts in spintronics are translated into the framework of Dirac and Weyl fermions. Note that a 3D Dirac fermion is composed of two Weyl fermions with left and right chiralities. The chiral density, i.e. the population difference between the two Weyl fermions, is weakly conserved in bismuth due to a small mass term that mixes the two Weyl fermions. This situation is analogous to

spintronics, where spin-orbit coupling causes the total number of spin to be non-conserved.

The magnetic proximity effect in spintronics is then translated into a localized background chiral gauge field (CGF) $A^5(x)$ spatially varying. The system under consideration is illustrated in Fig. 1(a), extending to x > 0 with the CGF localized near the interface at x = 0 and pointing in the z direction. We interpret the change in the background CGF as the "spin current" running in the x direction. Notice that this interpretation is valid even for spin nonconserving processes.

An additional critical component for generating a charge current is a counterpart to the "dissipative spin current" discussed in Ref. [6]. We interpret this as a dissipative flow toward the bulk, represented by a gradient in certain thermodynamic quantities. Specifically, we consider two candidates: (i) chemical potential $\mu(x)$, and (ii) inverse temperature $\beta(x)$ that alter in the x-direction. Below, we demonstrate that the gradients of these two thermodynamic quantities lead to charge currents in the y direction, each with a distinct dependency on fermionic density. One reason for selecting these two quantities is that they give rise to transport phenomena in Weyl semimetals induced by (i) the chiral anomaly and (ii) the gravitational anomaly, respectively [8–12].

It is natural to conceive that a chiral magnetic field \mathbf{B}^5 induced by the CGF, $\mathbf{B}^5 = \nabla \times \mathbf{A}^5$, generates a charge current in the bulk according to the chiral magnetic effect (CME) [13, 14]. In our setup with $\mathbf{B}^5 = (0, B_y^5, 0)$, this charge current runs in the y direction and CME gives $J_y = B_y^5 \mu_{\text{CLL}}/2\pi^2$, where μ_{CLL} is the chemical potential of the bulk state. However, this is only half of the story. There exists another current contribution from the boundary state, and the thermodynamic gradients lead to an imbalance between the two contributions. In addition, the CME expression does not account for temperature dependence. As we will show, the total charge current has the following general form,

$$J_{y} = \frac{1}{2\pi^{2}}\alpha(\mu, \beta, \Lambda)B_{y}^{5},$$

where the coefficient α involves the chemical potential μ and the inverse temperature β around the bulk and boundary states, and an ultraviolet (UV) cutoff Λ as well (see Eq. (7) for the result). A similar expression is derived for the total energy

^{*} teh@issp.u-tokyo.ac.jp

[†] oka@issp.u-tokyo.ac.jp

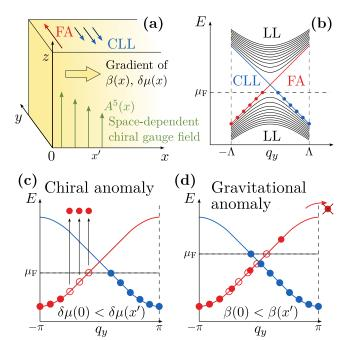


FIG. 1. (a) Key components for achieving a finite anomalous current along the y direction at one boundary. x' denotes the position where the CLL state is located at. (b) Dispersion of the FA, CLL, and LL states in the presence of chiral magnetic field. Λ is a UV cutoff parameter below which the continuum Dirac model in Eq. (1) becomes a good description. (c) Chiral anomaly-like scenario: The imbalance of the electron population is generated by the chemical potential gradient $\delta \mu(x)$. (d) Gravitational anomaly-like scenario: The temperature gradient $\beta(x)$ leads to different spreads of electrons. The boundary of Brillouin zone gives rise to the distinct current contributions from the two chiral states — part of the FA electron does not contribute to the current. The corresponding transport formulas for the two scenarios are derived in Eqs. (7)-(9).

current (see [15] for details).

Dirac Hamiltonian and Chiral Gauge Field — We consider the general Dirac Hamiltonian with a background CGF,

$$H = v \sum_{i} \gamma^0 \gamma^j q_j + m \gamma^0 + \sum_{i} A_j^5 \gamma^0 \gamma^j \gamma^5, \tag{1}$$

where the Latin index j runs over the three space coordinates and q_j is the corresponding momentum. v denotes the Fermi velocity, m labels the Dirac mass, and A_j^5 is the strength of the background CGF in the j-th direction. $\{\gamma^\mu\}$ represent the standard gamma matrices satisfying Clifford algebra, with the Greek index μ labeling the spacetime coordinates. In this paper, we apply the chiral representation for the gamma matrices, namely $\gamma^0 = [0\,I;\,I\,0]$ and $\gamma^j = [0\,\sigma^j;\,-\sigma^j\,0]$ where I and σ^j denote the identity and the j-th component of Pauli matrices.

Microscopically, there are several origins for the CGF: (i) Spin polarization induced by magnetic electrodes or surface magnetization through irradiating a circularly polarized laser [16], (ii) Floquet-induced CGF [17, 18], and (iii) lattice distortion [19, 20]. When the system is homogeneous and the CGF is large enough, i.e. $|\mathbf{A}^5| > m$, the Dirac cone splits into

a pair of Weyl cones due to the breakdown of time-reversal symmetry, and Fermi arc (FA) states appear on the surfaces. The Weyl nodes are topologically protected, and various microscopic models for Weyl semimetals have been proposed in prior research [21–23], with their transports also being intensively studied [9, 14, 24–33].

Inspired by experiments, we also allow in the CGF for a space dependency. This space dependency leads to an effective chiral magnetic field, $\mathbf{B}^5 = (0, B_y^5, 0)$ in our setup, which further induces Landau levels (LLs) and a chiral Landau level (CLL) as shown in Fig. 1(b) [34]. As we will show, an additional thermodynamic gradient creates an imbalance between the two chiral states as schematically summarized in Figs. 1(c) and 1(d). In contrast to the mixed axial–gravitational anomaly, which requires collinear (chiral) magnetic field and thermal gradient for obtaining a nonzero charge current [35–37], our thermal gradient needs to point away from the chiral magnetic field.

Lattice Model — To study edge properties of Eq. (1) and calculate current, we construct the following lattice model [38],

$$H = \sum_{l=1}^{L} \left\{ \left[v \sum_{j=y,z} \gamma^{0} \gamma^{j} \sin(q_{j} + A_{j}) + M(\mathbf{q}) \gamma^{0} \right] c_{l}^{\dagger} c_{l} + v \gamma^{0} \gamma^{x} \frac{1}{2i} \left(e^{iA_{x}} c_{l}^{\dagger} c_{l+1} - e^{-iA_{x}} c_{l}^{\dagger} c_{l-1} \right) - \lambda \gamma^{0} \left(e^{iA_{x}} c_{l}^{\dagger} c_{l+1} + e^{-iA_{x}} c_{l}^{\dagger} c_{l-1} \right) + A_{z}^{5}(x) \gamma^{0} \gamma^{z} \gamma^{5} c_{l}^{\dagger} c_{l} \right\},$$
(2)

where $M(\mathbf{q}) = m + 6\lambda - 2\lambda[\cos{(q_y + A_y)} + \cos{(q_z + A_z)}]$, and ν represents the Fermi velocity. We implement open boundaries in the x direction where the lattice site is labeled by l, and there are L sites in total. We introduce the electron hopping integral λ to gap out all the degeneracies at the boundary of Brillouin zone. We intentionally include the vector gauge field A_j so that we can calculate the current operator later. Without loss of generality, we restrict the CGF to pointing in the z direction. The Dirac Hamiltonian in Eq. (1) is recovered in the small q_j limit. Hereafter our primary focus is on the massless situation since the results change only quantitatively when m is small (see Fig. 3(d) for the mass dependency).

Chiral States — In Fig. 2(a), we show the eigenenergies obtained by exact diagonalization for Eq. (2) when $A_z^5(x) = A^5$ is constant. As expected, two FA states emerge and localize at x = 0 and x = L. The localized wave function $\psi_{FA}(x)$ can be obtained by solving Schrödinger equation for the continuum model of Eq. (1) (replacing q_x with $-i\partial_x$). Near the boundary x = 0, specifically for $A^5 > 0$, the wave function takes the form [25],

$$\psi_{\text{FA}} \sim \begin{bmatrix} e^{(q_z - A^5/v)x} c_{\text{L}} \\ e^{(q_z - A^5/v)x} (-ic_{\text{L}}) \\ e^{(-q_z - A^5/v)x} c_{\text{R}} \\ e^{(-q_z - A^5/v)x} ic_{\text{R}} \end{bmatrix},$$
(3)

and the corresponding eigenenergy is $E = vq_y$. The normalization coefficients $c_{L,R}$ satisfy $c_R = \pm ic_L$ due to the particle-

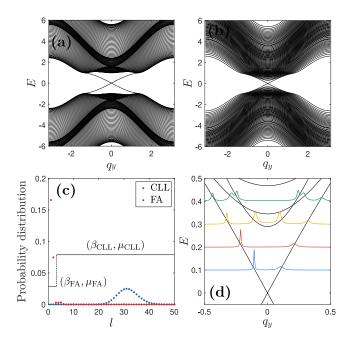


FIG. 2. (a) Band structures of the lattice Hamiltonian in Eq. (2) with a constant CGF A_z^5 , and (b) with a gradient CGF $A_z^5(x)$. Parameters used in the calculations are: $\Omega=0.1, v=1, m=0, \lambda=-1, L=\xi=50$, and $A^5=1.6$. The band structure in (b) has the same chiral state eigenenergies as in (a), but involves more intricate LL structures. (c) Real space probability densities of the two chiral states obtained in (b) at $q_y=0.8$. When the CGF becomes space-dependent, one FA state stays localized at the boundary (red dots), and the other turns into a CLL state, delocalizing in the bulk (blue dots). Black lines are effective inverse temperatures and chemical potentials considered in the derivation of Eq. (7). (d) Calculations for spectral function (color lines) at different energies of the spectrum in Fig. 1(b). The CLL state remains more robust against the scattering than the FA state. The impurity strength $\kappa=0.02$.

hole symmetry of Eq. (2), $\gamma^x H(q_y,q_z)(\gamma^x)^\dagger = -H(-q_y,-q_z)$ at $\mathbf{A}=0$, and the sign \pm is determined by the parameters used in the lattice Hamiltonian. A normalizable solution exists only when $-A^5 < vq_z < A^5$. Note that the Hermiticity condition derived at the boundary is satisfied for this solution [39], $\psi_{\mathrm{FA}}^\dagger \gamma^0 \gamma^1 \psi_{\mathrm{FA}}|_{x=0} = 0$, indicating that a net current running in the x direction is forbidden. The other FA state can be solved in a similar way and it acquires an eigenenergy $E = -vq_y$. The emergence of these FA states localized at the two boundaries requires a homogeneous background CGF throughout the entire sample.

By contrast, in the following we consider a localized A_z^5 field leading to two topologically protected chiral states as well but only one boundary is needed. We set $A_z^5(x) = A^5(1 - x/\xi)\Theta(\xi - x)$ where Θ is the Heaviside step function and ξ is a cutoff. In Fig. 2(b), we show the resulting spectrum which shares the same linear dispersion $E = \pm vq_y$ near $q_y = 0$ as in Fig. 2(a). However, there are two differences: First, the bulk spectrum in Fig. 2(b) has additional LL structures. Second, one of the chiral states in Fig. 2(a) is no longer a FA state. As shown in Fig. 2(c), it leaks into the bulk and becomes a CLL state. Both differences can be attributed to

the effective chiral magnetic field \mathbf{B}^5 . We use the canonical quantization to solve Schrödinger equation in the presence of \mathbf{B}^5 , and obtain the CLL wavefunction (see [15] for details),

$$\psi_{\text{CLL}} \sim \begin{bmatrix} e^{-A^5 x^2 / 2 v \xi + (-q_z + A^5 / v) x} (-c_{\text{L}}) \\ e^{-A^5 x^2 / 2 v \xi + (-q_z + A^5 / v) x} (-ic_{\text{L}}) \\ e^{-A^5 x^2 / 2 v \xi + (q_z + A^5 / v) x} (ic_{\text{R}}) \\ e^{-A^5 x^2 / 2 v \xi + (q_z + A^5 / v) x} c_{\text{R}} \end{bmatrix},$$
(4)

with an eigenenergy $E_0 = -vq_y$ unchanged from the FA state. The normalization coefficients $c_{\rm L}$ and $c_{\rm R}$ satisfy $c_{\rm R} = \pm ic_{\rm L}$ due to the particle-hole symmetry. The sign \pm also hinges on the parameters of the Hamiltonian. The delocalized Gaussian characteristic of the CLL state raises concerns that it might be strongly destroyed by impurities.

Robustness of CLL — We check the robustness of the CLL state by considering disorders through a self-energy under the first Born approximation [40], $\Sigma^{\text{FBA}}(\omega) = \int dq_y dq_z \, 1/\left[\omega + i\eta - H(q_y, q_z)\right]$ at frequency ω . For simplicity, we require the impurities to be much heavier than the electron so that the electron is scattered locally, and we assume that the scattering is independent on orbitals labeled by ν . That being said, we consider the retarded self-energy to be $\Sigma^{\text{R}}_{l\nu,l',\nu'}(\omega) = \kappa \Sigma^{\text{FBA}}_{l\nu,l\nu} \delta_{ll'} \delta_{\nu\nu'}$, where κ represents the impurity strength.

We proceed by calculating the spectral function $A(\omega) = (-1/\pi) \text{Im} \left\{ \int dq_1 dq_2 \, \text{Tr} \left\{ G^R \right\} \right\}$ to see the broadening of the dispersion. The retarded Green function is $G^R = 1/(\omega + i\eta - H - \Sigma^R)$. In Fig. 2(d), we plot the spectral function at different frequencies with different colors. Remarkably, we find much smaller lifetime for FA dispersion than the CLL dispersion, manifesting that CLL state is topologically protected as well.

Anomalous Current and Its Fermi Level Dependency — We now focus on the two scenarios depicted in Fig. 1(c) and 1(d) (no impurity), numerically calculating the current in the y direction by [41, 42]

$$\langle J_y \rangle = \frac{1}{2\pi i} \int_{-\infty}^{\infty} d\omega \int \frac{dq_y dq_z}{(2\pi)^2} \operatorname{Tr} \{ J_y G^{<} \}, \tag{5}$$

where $G^<$ is the lesser Green function, and the current operator is obtained by taking the variation of the lattice Hamiltonian $J_y = -\delta H/\delta A_y|_{A=0}$. In order to apply the chemical potential/temperature gradients, we utilize the standard nonequilibrium Green function technique for calculating $G^< = G^R \Sigma^< G^A$. The advanced Green function G^A is Hermitian adjoint of G^R . The retarded self-energy Σ^R and the lesser self-energy $\Sigma^<$ describe how the system couples to fictitious electron baths which we use to implement chemical potential/temperature gradients. We consider $\Sigma^R = -i\Gamma/2$ and $\Sigma^<_{ll'} = i\Gamma f(\omega,\beta_l,\mu_l)\delta_{ll'}$ where the standard wide-band limit approximation and a constant tunneling strength Γ are applied. We also require independent electron baths coupled to each site, and the electron bath follows the Fermi-Dirac distribution $f(\omega,\beta_l,\mu_l)$ with site-dependent chemical potential μ_l and inverse temperature β_l .

In the small Γ limit, Eq. (5) becomes

$$\langle J_y \rangle = \frac{1}{i\Gamma} \int_{-\pi}^{\pi} \frac{dq_y dq_z}{(2\pi)^2} \sum_{\alpha} \langle \alpha | J_y | \alpha \rangle \langle \alpha | \Sigma^{<}(E_{\alpha}) | \alpha \rangle, \quad (6)$$

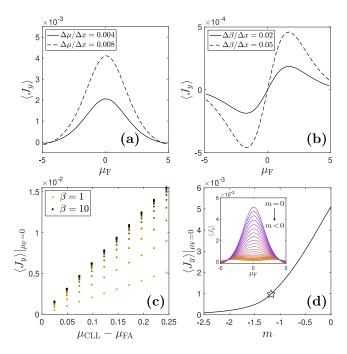


FIG. 3. (a)(b) Numerical calculations for the anomalous current as a function of Fermi level $\mu_{\rm F}$ when (a) a chemical potential gradient is applied at a fixed $\beta=1$, and (b) when a temperature gradient is included ($\beta_0=1$). The current results show even and odd symmetry under different thermodynamic gradients. Other parameters are the same as those used in Fig. 2(b). (c) Temperature dependency of $\langle J_y \rangle$ as a function of $\mu_{\rm CLL}-\mu_{\rm FA}$ in the chiral anomaly-like scenario. Ten values of $\beta=1,2,...,10$ are included with different colors (from light to dark). The linear dependence at each temperature and the asymptotic behavior approaching the low temperature limit are consistent with Eq. (8). (d) Mass dependency of $\langle J_y \rangle$. Gap opens around m=-1.2 labeled by the star. The current becomes smaller when |m| is larger, but remains finite even in the trivial phase .

where Lehmann representation $H|\alpha\rangle = E_{\alpha}|\alpha\rangle$ is applied. In Fig. 3(a) we show numerical current results of the chiral anomaly-like scenario by using Eq. (6): We consider a linear gradient of the chemical potential $\mu_l = (\Delta \mu / \Delta x)(l - L/2 +$ 1/2) + $\mu_{\rm F}$, where $\Delta \mu / \Delta x$ denotes the slope and $\mu_{\rm F}$ represents the Fermi level, under a constant temperature $\beta_l = \beta$. In Fig. 3(b) we provide current results of the gravitational anomaly-like scenario: We consider a constant chemical potential $\mu_l = \mu_F$ but with a linear increase of the inverse temperature $\beta_l = \beta_0 + (\Delta \beta / \Delta x) l / L$, where β_0 is the inverse temperature on the surface and $\Delta \beta / \Delta x$ represents the slope. We find that nonzero anomalous currents appear in both nonequilibrium cases, and the two scenarios exhibit distinct characteristics (odd and even functions). In fact, both signatures have been observed in the experiment [7], where the measurable electron density n is related to the Fermi energy $\mu_{\rm F}$ through $\mu_{\rm F} \propto n^{2/3}$.

Transport Formula — To understand the underlying mechanism of the anomalous current, we follow the derivation of the anomaly-induced transport [8], constructing an effective two-band model of FA and CLL states to illustrate the low energy physics near the crossing points. For α =

{FA, CLL}, $\langle \alpha | J_y | \alpha \rangle = \pm v$ and $E_\alpha = \pm v q_y$ in Eq. (6). For simplicity, as schematically shown in Fig. 2(c), we consider a localized chemical potential $\mu(x)$ and a localized inverse temperature $\beta(x)$ such that: $\{\mu(x), \beta(x)\} = \{\mu_{FA}, \beta_{FA}\}$ when $x < l^{FA}$, where l^{FA} is the delocalization length of the FA state, and $\{\mu(x), \beta(x)\} = \{\mu_{CLL}, \beta_{CLL}\}$ elsewhere. By doing so, the matrix element of the lesser self-energy for the FA state becomes, $\langle FA|\Sigma^{<}|FA\rangle = \sum_{ll'}^{L} \langle FA|l \rangle \langle \Sigma^{<}\rangle_{ll'} \langle l'|FA\rangle = i\Gamma f(E_{FA}, \beta_{FA}, \mu_{FA})$, where $\langle l|FA\rangle$ represents the FA wavefunction at the l-th site. Similarly, for the CLL state, $\langle CLL|\Sigma^{<}|CLL\rangle = i\Gamma f(E_{CLL}, \beta_{CLL}, \mu_{CLL})$. As a result, Eq. (6) becomes

$$\langle J_y \rangle = \frac{A^5}{2\pi^2} \left(\mu_{\text{CLL}} \tanh \frac{\beta_{\text{CLL}} \nu \Lambda}{2} - \mu_{\text{FA}} \tanh \frac{\beta_{\text{FA}} \nu \Lambda}{2} \right), \quad (7)$$

plus $O(\mu_{\rm CLL}^3, \mu_{\rm FA}^3)$. Note that $A^5 = -B_y^5 L$, and the chiral states are estimated to exist along the q_z coordinate within the range $[-A^5, A^5]$. Additionally, since the integrand in Eq. (6) does not depend on q_z , the asymmetry between the two chiral states solely comes from the integral over q_y , as depicted in Fig. 1(c) and 1(d).

A finite current can be obtained when either $\mu_{FA} \neq \mu_{CLL}$ or $\beta_{FA} \neq \beta_{CLL}$ (or both). On one hand, when $\beta_{FA} = \beta_{CLL} = \beta$, Eq. (7) reduces to

$$\langle J_y \rangle = \frac{A^5}{2\pi^2} \tanh\left(\frac{\beta v \Lambda}{2}\right) (\mu_{\text{CLL}} - \mu_{\text{FA}}),$$
 (8)

which shows an even function of μ_F as in Fig. 3(a) (set $\mu_{FA} = \mu_F - \delta$, $\mu_{CLL} = \mu_F + \delta$, and see $\langle J_y \rangle$ is independent of μ_F). On the other hand, when $\mu_{FA} = \mu_{CLL} = \mu_F$, Eq. (7) becomes

$$\langle J_y \rangle = \frac{A^5}{2\pi^2} \left(\tanh \frac{\beta_{\text{CLL}} v \Lambda}{2} - \tanh \frac{\beta_{\text{FA}} v \Lambda}{2} \right) \mu_{\text{F}},$$
 (9)

which verifies the odd-function profile in Fig. 3(b). Most importantly, while the UV completion $\Lambda \to \infty$ is usually taken in both high energy and condensed matter literature, leading to $\langle J_y \rangle \to (A^5/2\pi^2)(\mu_{\rm CLL} - \mu_{\rm FA})$ in Eq. (8) and $\langle J_y \rangle \to 0$ in Eq. (9), our calculations demonstrate the importance of a careful treatment for the cutoff Λ — We would not get the temperature dependence in Eq. (8) and a finite current in Eq. (9) if we simply take the UV limit. Note that the UV limit of Eq. (8) is the generalized CME result involving both the bulk and boundary current contributions, and the temperature dependence as well. For completeness, we also derive an analogous expression to Eq. (7) for the energy current, as details provided in [15]. There we also find two contributions to the energy current — One from the surface FA state and the other from the bulk CLL state, and a careful treatment of the UV cutoff also reveals additional components.

Finally we investigate the temperature dependence of the lattice calculation by using Eq. (6), and check the consistency to Eq. (8). We focus on $\mu_F = 0$ and simulate different values of $\Delta\mu/\Delta x$ and β . Following Fig. 2(c), we assign the value of chemical potential at 0th site to μ_{FA} , and use μ_F as an approximate μ_{CLL} , since the Gaussian-profile CLL state homogeneously delocalizes around the real space over different values of q_z . In Fig. 3(c), we find clearly linear dependency of

 $\langle J_y \rangle$ on $\mu_{\text{CLL}} - \mu_{\text{FA}}$ and the data points asymptotically approach a fixed line at low temperature. These findings are in line with Eq. (8).

Mass dependency — In Fig. 3(d), we plot $\langle J_y \rangle$ at $\mu_F = 0$ as a function of mass, ranging from massless to the massive topologically trivial phase (phase transition occurs around m=-1.2). In the topological phase, the current depends on the length of flat band region along the q_z direction, corresponding to the integral over q_z in Eq. (7). The current decreases as |m| increases; however, it remains finite even in the trivial phase. The result suggests that the ISHE can be substantially enhanced in the massless case.

Conclusion — We numerically and analytically demonstrate the existence of anomalous charge currents in the three dimensional Dirac fermionic systems when two crucial elements are applied: A background CGF, which we allow to be space dependent, and a thermodynamic gradient. We establish a connection between these elements and the necessary components in the ISHE. The charge currents as a function of the Fermi level are even and odd symmetric in the presence of the chemical potential gradient and the temperature gradient, respectively. Microscopically the finite anomalous currents are generated by the imbalance between the two chiral states — the FA state localized at the boundary and the delocalized CLL state induced by the space dependency of the CGF. We numer-

ically verify that the CLL state is actually more robust against impurity than the FA state. Additionally, we derive the transport formula Eq. (7) for the anomalous current, from which we argue that only when we carefully keep the UV cutoff can we explain the lattice calculations. A similar expression for the energy current is also provided.

Inspired by Ref. [43], we have also investigated a non-Hermitian anomaly-like scenario where we apply an inhomogeneous tunneling strength Γ_l as a function of site. To our surprise, no anomalous current is observed, even with artificial negative lifetimes for partial sites. It is worth stressing that our findings align with recent experimental observations, indicating that our model can be potentially considered as a microscopic candidate for the ISHE.

ACKNOWLEDGEMENT

The authors appreciate the fruitful discussions with Y. Araki, Y. Fuseya, M. Hayashi, T. Morimoto, K. Nomura, A. Ozawa, and G. Tatara. This work is supported by JST CREST Grant No. JPMJCR19T3, Japan. S.O. is supported by JSPS KAKENHI Grants Nos. JP22K13998 and JP23K25816.

- [1] M. Dyakonov and V. Perel, Current-induced spin orientation of electrons in semiconductors, Phys. Lett. A **35**, 459 (1971).
- [2] J. E. Hirsch, Spin hall effect, Phys. Rev. Lett. 83, 1834 (1999).
- [3] S. Zhang, Spin hall effect in the presence of spin diffusion, Phys. Rev. Lett. 85, 393 (2000).
- [4] J. Sinova, D. Culcer, Q. Niu, N. A. Sinitsyn, T. Jungwirth, and A. H. MacDonald, Universal intrinsic spin hall effect, Phys. Rev. Lett. 92, 126603 (2004).
- [5] S. Murakami, N. Nagaosa, and S.-C. Zhang, Dissipationless quantum spin current at room temperature, Science 301, 1348 (2003).
- [6] E. Saitoh, M. Ueda, H. Miyajima, and G. Tatara, Conversion of spin current into charge current at room temperature: Inverse spin-Hall effect, Appl. Phys. Lett. **88**, 182509 (2006).
- [7] M. Kawaguchi, H. Hirose, Z. Chi, Y.-C. Lau, F. Freimuth, and M. Hayashi, Giant inverse faraday effect in dirac semimetals, arXiv:2009.01388 (2020).
- [8] K. Landsteiner, Notes on anomaly induced transport, arXiv:1610.04413 (2016).
- [9] A. A. Zyuzin and A. A. Burkov, Topological response in weyl semimetals and the chiral anomaly, Phys. Rev. B 86, 115133 (2012).
- [10] A. Burkov, Chiral anomaly and transport in weyl metals, J. Phys. Condens. Matter 27, 113201 (2015).
- [11] J. Behrends, S. Roy, M. H. Kolodrubetz, J. H. Bardarson, and A. G. Grushin, Landau levels, bardeen polynomials, and fermi arcs in weyl semimetals: Lattice-based approach to the chiral anomaly, Phys. Rev. B 99, 140201 (2019).
- [12] M. N. Chernodub, Y. Ferreiros, A. G. Grushin, K. Landsteiner, and M. A. Vozmediano, Thermal transport, geometry, and anomalies, Phys. Rep. 977, 1 (2022).

- [13] K. Fukushima, D. E. Kharzeev, and H. J. Warringa, Chiral magnetic effect, Phys. Rev. D 78, 074033 (2008).
- [14] D. E. Kharzeev, The chiral magnetic effect and anomaly-induced transport, Prog. Part. Nucl. Phys. **75**, 133 (2014).
- [15] See Supplemental Material for "Chiral Landau Level State" and "Energy Current".
- [16] Y. Araki, A. Yoshida, and K. Nomura, Universal charge and current on magnetic domain walls in weyl semimetals, Phys. Rev. B 94, 115312 (2016).
- [17] S. Ebihara, K. Fukushima, and T. Oka, Chiral pumping effect induced by rotating electric fields, Phys. Rev. B 93, 155107 (2016).
- [18] N. Yoshikawa, Y. Hirai, K. Ogawa, S. Okumura, K. Fujiwara, J. Ikeda, T. Koretsune, R. Arita, A. Mitra, A. Tsukazaki, T. Oka, and R. Shimano, Light-induced chiral gauge field in a massive 3d dirac electron system, arXiv:2209.11932 (2022).
- [19] A. Cortijo, Y. Ferreirós, K. Landsteiner, and M. A. H. Vozmediano, Elastic gauge fields in weyl semimetals, Phys. Rev. Lett. 115, 177202 (2015).
- [20] D. I. Pikulin, A. Chen, and M. Franz, Chiral anomaly from strain-induced gauge fields in dirac and weyl semimetals, Phys. Rev. X 6, 041021 (2016).
- [21] X. Wan, A. M. Turner, A. Vishwanath, and S. Y. Savrasov, Topological semimetal and fermi-arc surface states in the electronic structure of pyrochlore iridates, Phys. Rev. B 83, 205101 (2011).
- [22] A. A. Burkov and L. Balents, Weyl semimetal in a topological insulator multilayer, Phys. Rev. Lett. 107, 127205 (2011).
- [23] N. P. Armitage, E. J. Mele, and A. Vishwanath, Weyl and dirac semimetals in three-dimensional solids, Rev. Mod. Phys. 90, 015001 (2018).

- [24] C.-X. Liu, P. Ye, and X.-L. Qi, Chiral gauge field and axial anomaly in a weyl semimetal, Phys. Rev. B 87, 235306 (2013).
- [25] P. Goswami and S. Tewari, Axionic field theory of (3 + 1)dimensional weyl semimetals, Phys. Rev. B 88, 245107 (2013).
- [26] D. T. Son and B. Z. Spivak, Chiral anomaly and classical negative magnetoresistance of weyl metals, Phys. Rev. B 88, 104412 (2013).
- [27] M. M. Vazifeh and M. Franz, Electromagnetic response of weyl semimetals, Phys. Rev. Lett. 111, 027201 (2013).
- [28] S. A. Parameswaran, T. Grover, D. A. Abanin, D. A. Pesin, and A. Vishwanath, Probing the chiral anomaly with nonlocal transport in three-dimensional topological semimetals, Phys. Rev. X 4, 031035 (2014).
- [29] T. Morimoto, S. Zhong, J. Orenstein, and J. E. Moore, Semiclassical theory of nonlinear magneto-optical responses with applications to topological dirac/weyl semimetals, Phys. Rev. B 94, 245121 (2016).
- [30] Z. Wang and S.-C. Zhang, Chiral anomaly, charge density waves, and axion strings from weyl semimetals, Phys. Rev. B 87, 161107 (2013).
- [31] P. Hosur, S. A. Parameswaran, and A. Vishwanath, Charge transport in weyl semimetals, Phys. Rev. Lett. 108, 046602 (2012).
- [32] R. Lundgren, P. Laurell, and G. A. Fiete, Thermoelectric properties of weyl and dirac semimetals, Phys. Rev. B 90, 165115 (2014).
- [33] A. Lucas, R. A. Davison, and S. Sachdev, Hydrodynamic theory of thermoelectric transport and negative magnetoresistance in weyl semimetals, Proc. Natl. Acad. Sci. 113, 9463 (2016).
- [34] A. G. Grushin, J. W. F. Venderbos, A. Vishwanath, and R. Ilan, Inhomogeneous weyl and dirac semimetals: Transport in axial magnetic fields and fermi arc surface states from pseudo-landau levels, Phys. Rev. X 6, 041046 (2016).
- [35] K. Landsteiner, E. Megías, and F. Pena-Benitez, Gravitational anomaly and transport phenomena, Phys. Rev. Lett. 107, 021601 (2011).
- [36] J. Gooth, A. C. Niemann, T. Meng, A. G. Grushin, K. Landsteiner, B. Gotsmann, F. Menges, M. Schmidt, C. Shekhar, V. Süß, R. Hühne, B. Rellinghaus, C. Felser, B. Yan, and K. Nielsch, Experimental signatures of the mixed axial-gravitational anomaly in the weyl semimetal nbp, Nature 547, 324 (2017).
- [37] K. Das and A. Agarwal, Thermal and gravitational chiral anomaly induced magneto-transport in weyl semimetals, Phys. Rev. Res. 2, 013088 (2020).
- [38] B. A. Bernevig, T. L. Hughes, and S.-C. Zhang, Quantum spin hall effect and topological phase transition in hgte quantum wells, Science **314**, 1757 (2006).
- [39] K. Hashimoto, T. Kimura, and X. Wu, Boundary conditions of Weyl semimetals, Prog. Theor. Exp. Phys. 2017, 053I01 (2017).
- [40] H. Bruus and K. Flensberg, Many-body quantum theory in condensed matter physics: an introduction (OUP Oxford, 2004).
- [41] H. Haug, A.-P. Jauho, et al., Quantum kinetics in transport and optics of semiconductors, Vol. 2 (Springer, 2008).
- [42] G. Stefanucci and R. Van Leeuwen, Nonequilibrium many-body theory of quantum systems: a modern introduction (Cambridge University Press, 2013).
- [43] K. Kawabata, K. Shiozaki, and S. Ryu, Topological field theory of non-hermitian systems, Phys. Rev. Lett. 126, 216405 (2021).
- [44] R. Loganayagam and P. Surówka, Anomaly/transport in an ideal weyl gas, J. High Energy Phys. **2012** (4), 1.

Appendix A: Chiral Landau Level State

In this section we provide details of deriving the chiral Landau level state, namely Eq. (4) in the main body of the text. When m=0, Eq. (1) in the main body of the text becomes block diagonal $H=[H_{\rm L}\,0;\,0\,H_{\rm R}]$ where L/R label left/right Weyl fermions, and $H_{\rm L,R}=\mp v\sum_j q_j\sigma^j+A_z^5(x)\sigma^z$. We first quantize the mechanical momenta in $H_{\rm L}$ by

$$\pi_x = -vq_x = \sqrt{B^5 v/2} (a + a^{\dagger})$$

$$\pi_z = -vq_z + A^5 (1 - x/\xi) = i \sqrt{B^5 v/2} (a - a^{\dagger}),$$

where the ladder operators satisfy $[a, a^{\dagger}] = 1$. The left Weyl Hamiltonian then becomes

$$H_{\rm L} = \pi_x \sigma^x - v q_v \sigma^y + \pi_z \sigma^z.$$

The eigenvalue problem can be solved, in a slightly easier way, by first rewriting $H_{\rm L}$ in the eigen basis of $\sigma^{\rm y}$: $H_{\rm L}' = U_{\rm y}^{\dagger} H_{\rm L} U_{\rm y}$ where $U_{\rm y} = [i\,i;\,-1\,1]/\sqrt{2}$. $H_{\rm L}'$ has eigenstates

$$|\psi_n'\rangle \sim \begin{bmatrix} u_n|n\rangle \\ v_n|n-1\rangle \end{bmatrix}$$

with bulk spectra $E_n = \pm \sqrt{2B^5vn + v^2q_y^2}$ for $n \ge 1$ (See Fig. 1(b) black lines in the main body of the text). Here $u_n, v_n \in \mathbb{C}$. The harmonic mode $|n\rangle$ satisfies $a|n\rangle = \sqrt{n}|n-1\rangle$ and $a^{\dagger}|n\rangle = \sqrt{n+1}|n+1\rangle$.

In addition, $H_{\rm L}'$ has a 0th chiral Landau level (CLL) eigenstate

$$|\psi_0'\rangle \sim \begin{bmatrix} u_0|0\rangle\\0 \end{bmatrix}$$

with eigenenergy $E_0 = -vq_y$ (See Fig. 1(b) blue line in the main body of the text). Note that the dispersion along the q_z direction remains flat bands for the (chiral) LL states.

The CLL wave function in real space can be obtained by solving

$$\langle x|a|\psi_0'\rangle \sim \begin{bmatrix} \langle x|au_0|0\rangle \\ 0 \end{bmatrix} = 0,$$

meaning that

$$\langle x|a|0\rangle = \sqrt{\frac{1}{2B^5v}} \langle x| (\pi_x - i\pi_z) |0\rangle$$

$$= \sqrt{\frac{1}{2B^5v}} \left[iv\partial_x - iA^5 \left(1 - \frac{x}{\xi} \right) + ivq_z \right] \phi_0^{\rm L}(x)$$

$$= 0,$$

where $\phi_0^{L}(x) = \langle x|0\rangle$. The solution is a Gaussian distribution

$$\phi_0^{\rm L}(x) \sim e^{-A^5 x^2/2\nu\xi + (-q_z + A^5/\nu)x}$$
.

Through the similar procedures, we obtain the same bulk and chiral spectra for the right Weyl Hamiltonian H_R , though the corresponding Gaussian distribution has a slightly different center:

$$\phi_0^{\rm R}(x) \sim e^{-A^5 x^2/2v\xi + (q_z + A^5/v)x}$$
.

As a result, we can combine the solutions for $H_{L/R}$ to obtain the 0th CLL state of the total Hamiltonian H. After transforming back to the eigen basis of σ^z , we get Eq. (4) in the main body of the text.

Appendix B: Energy Current

In this section we derive the energy current, which is analogous to the charge current in Eq. (7) in the main body of the text, for the effective two band model of the FA and CLL states. The derivation follows similar procedure to achieve Eq. (7) in the main text, except that the charge current operator J_y is replaced by the energy current operator J_y^E ,

$$\langle J_y^{\rm E} \rangle = \frac{1}{i\Gamma} \int_{-\pi}^{\pi} \frac{dq_y dq_z}{(2\pi)^2} \; \sum_{\alpha} \langle \alpha | J_y^{\rm E} | \alpha \rangle \langle \alpha | \Sigma^<(E_\alpha) | \alpha \rangle. \label{eq:energy_equation}$$

In relativistic theory, $\langle \alpha | J_y^{\rm E} | \alpha \rangle = q_y$ for $\alpha = \{{\rm FA, CLL}\}$, and therefore,

$$\begin{split} \langle J_{y}^{E} \rangle &= \frac{A^{5}}{2\pi^{2}} \int_{-\Lambda}^{\Lambda} dq_{y} \Big\{ q_{y} f(E_{\text{FA}}, \beta_{\text{FA}}, \mu_{\text{FA}}) \\ &+ q_{y} f(E_{\text{CLL}}, \beta_{\text{CLL}}, \mu_{\text{CLL}}) \Big\} \\ &= \frac{A^{5}}{2\pi^{2} v^{2}} \int_{-v\Lambda}^{v\Lambda} dx \, \left\{ \frac{x}{e^{\beta_{\text{FA}}(x - \mu_{\text{FA}})} + 1} - \frac{x}{e^{\beta_{\text{CLL}}(x - \mu_{\text{CLL}})} + 1} \right\}. \end{split}$$

The integral has the following closed form,

$$\langle J_{y}^{E} \rangle = \frac{A^{5}}{2\pi^{2}v^{2}} \Big[I \left(\beta_{FA}, \mu_{FA} \right) - I \left(\beta_{CLL}, \mu_{CLL} \right) \Big], \tag{B1}$$

where

$$\begin{split} I(\beta,\mu) &\equiv -\frac{v\Lambda}{\beta} \ln\left[\left(1+e^{-\beta v\Lambda}\right)\left(1+e^{\beta v\Lambda}\right)\right] \\ &+ \frac{1}{\beta^2} \left[\operatorname{Li}_2\left(-e^{-\beta v\Lambda}\right) - \operatorname{Li}_2\left(-e^{\beta v\Lambda}\right)\right] \\ &+ \left[-\frac{\beta v\Lambda e^{\beta v\Lambda}}{\left(e^{\beta v\Lambda}+1\right)^2} - \frac{1}{e^{\beta v\Lambda}+1} + \frac{1}{2}\right] \mu^2 + O(\mu^3). \end{split} \tag{B2}$$

Here Li₂ denotes the dilogarithm function. Equations (B1) and (B2) provide the general energy current expressions, which involve not only β and μ but also the UV cutoff Λ . In the UV limit where $\Lambda \to \infty$, we recover the chiral magnetic effect in the energy current [8, 44]:

$$\langle J_{y}^{\rm E} \rangle = \frac{A^{5}}{12\nu^{2}} \left(\frac{1}{\beta_{\rm EA}^{2}} - \frac{1}{\beta_{\rm CLL}^{2}} \right) + \frac{A^{5}}{4\nu^{2}\pi^{2}} \left(\mu_{\rm FA}^{2} - \mu_{\rm CLL}^{2} \right).$$

However, as demonstrated for the charge current in the main body of the text, the cutoff dependency is crucial for explaining the lattice calculations, so that the extra contribution must be carefully included.